***PREPRINT**: Blocken B, Carmeliet J. 2007. Validation of CFD simulations of wind-driven rain on a low-rise building facade. Building and Environment 42(7): 2530–2548. © Elsevier 2007.*

Validation of CFD simulations of wind-driven rain on a low-rise building facade

Bert Blocken* [(a)], Jan Carmeliet [(a,b)]

(a) Unit Building Physics and Systems, Faculty of Building and Architecture, Technische Universiteit Eindhoven, P.O. box 513, 5600 MB Eindhoven, the Netherlands
(b) Laboratory of Building Physics, Department of Civil Engineering, Katholieke Universiteit Leuven, Kasteelpark Arenberg 40, 3001 Leuven, Belgium

Abstract

For decades, the assessment of the amount and intensity of wind-driven rain (WDR) falling onto building facades has been performed either by measurements or by semi-empirical methods such as the WDR index and the WDR relationship. In the past fifteen years, numerical assessment methods based on Computational Fluid Dynamics (CFD) have secured their place in WDR research. Despite the widespread use of these methods at present, very few efforts have been made towards validation of CFD simulations of WDR on buildings. This paper presents a detailed validation study for a low-rise building of complex geometry, supported by a recently published, high-resolution full-scale wind, rain and WDR measurement dataset that was specifically created for CFD validation. It is shown that the CFD simulations can provide quite accurate predictions of the amount of WDR impinging on the building facade, for a number of very different rain events, and that the main discrepancies, in this study, are due to a simplification of the upstream wind conditions.

Keywords: Wind-driven rain; Driving rain; Air flow; Building; Numerical simulation; Computational Fluid Dynamics; CFD; Validation; Experimental data

1. Introduction

Three categories of methods exist for the assessment of wind-driven rain (WDR) on building facades: (1) measurements, (2) semi-empirical methods and (3) numerical methods based on Computational Fluid Dynamics (CFD). A literature review of each of these categories is provided in [1]. Measurements have always been the primary tool in WDR research, although a systematic experimental approach in WDR assessment is not feasible. Different reasons are responsible for this, the most important of which is the fact that WDR measurements can easily suffer from large errors [2-5]. Recently, guidelines that should be followed for selecting accurate and reliable WDR data from experimental WDR datasets have been proposed [4,5]. The strict character of these guidelines however implies that only very few rain events in a WDR dataset are accurate and reliable and hence suitable for WDR studies. Other drawbacks of WDR measurements are the fact that they are time-consuming and expensive and the fact that measurements on a particular building site have very limited application to other sites. These limitations drove researchers to establish semi-empirical relationships between the quantity of WDR and the influencing climatic parameters wind speed, wind direction and horizontal rainfall intensity (i.e. the rainfall intensity through a horizontal plane, as measured by a traditional rain gauge). The advantage of semi-empirical methods is their ease-of-use; their main disadvantage is that only rough estimates of the WDR exposure can be obtained [1]. Given the drawbacks associated with measurements and with semi-empirical methods, researchers realized that further achievements were to be found by employing numerical methods. In the past fifteen years, the introduction of Computational Fluid Dynamics (CFD) in the area has provided a new impulse in WDR research. Choi [6-8] developed a numerical simulation technique to determine the distribution of WDR on buildings under steady-state conditions of wind and rain. This technique has been universally adopted by the WDR research community.

Validation is an essential part of CFD simulations with turbulence models. Up to now, only a few attempts have been made towards the validation of CFD simulations of WDR [3,9,10]. Although these pioneering studies are very valuable and have provided the necessary basis for further research, they focused on single stationary rain events, i.e. single intervals with a fixed, static value of wind speed, wind direction and horizontal rainfall

* Corresponding author: Bert Blocken, Building Physics and Systems, Technische Universiteit Eindhoven, P.O.Box 513, 5600 MB Eindhoven, the Netherlands. Tel.: +31 (0)40 247 2138 - Fax: +31 (0)40 243 8595
E-mail address: b.j.e.blocken@tue.nl

intensity, which limited the validation capacity. In 2002, Blocken and Carmeliet [11] extended Choi's steady-state simulation technique into the time domain. The existing simulation technique was incorporated into a generalized numerical simulation model that allows determining the WDR distribution on building facades in space and in time. Due to this extension, it has now become possible to use measured wind, rain and WDR data (that are highly variable in time) for validation purposes. At the same time, a preliminary validation effort was conducted, based on measurements with a few WDR gauges on a low-rise building [11]. In 2004, the extended WDR simulation model by Blocken and Carmeliet was successfully used by Tang and Davidson [12] at the University of Pittsburg to study the WDR distribution on the high-rise Cathedral of Learning. The numerical simulation results obtained with this model were compared to the corresponding measurements made at different locations on the cathedral facades. Apart from these studies, no validation studies with the extended simulation model are known to the authors.

In this paper, a detailed validation study is performed for a low-rise building, supported by a high-resolution experimental WDR dataset obtained from a measurement set-up that was specifically designed for CFD validation studies [5]. For the validation study to be reliable, high quality of the experimental data is required, imposing demands on accuracy and reliability. The accuracy and reliability of the experimental dataset used here has been ensured by strictly following the WDR data selection guidelines that were provided in [4]. In section 2 of this paper, the definitions of the specific catch ratio and the catch ratio are provided and the influencing parameters of WDR are summarized. In section 3, the measurement set-up for wind, rain and WDR at the Laboratory of Building Physics is briefly described. Section 4 comprises a brief outline of the extended WDR simulation model. In sections 5 and 6, this model is applied to calculate the spatial and temporal distribution of WDR on the low-rise building facade and the numerical results are compared with the corresponding measurements. Section 7 (discussion) and section 8 (conclusions) conclude the paper.

2. Definitions and parameters

The quantities that are used to describe the WDR intensity are the specific catch ratio $\eta_d(d)$, related to the raindrop diameter d, and the catch ratio η, related to the entire spectrum of raindrop diameters (Eq. 1):

$$\eta_d(d,t) = \frac{R_{wdr}(d,t)}{R_h(d,t)} \quad ; \quad \eta(t) = \frac{R_{wdr}(t)}{R_h(t)} \tag{1}$$

where $R_{wdr}(d)$ and $R_h(d)$ are the specific WDR intensity on the building and the specific unobstructed horizontal rainfall intensity. R_{wdr} and R_h respectively refer to the same quantities but integrated over all raindrop diameters. The unobstructed horizontal rainfall intensity is the intensity of rainfall through a horizontal plane that is situated outside the wind-flow pattern that is disturbed by the building (i.e. the rainfall that would be measured by a rain gauge with a horizontal orifice at ground-level, placed in an open field). In practical applications the (specific) catch ratio will be measured and calculated for discrete time steps $[t_j, t_j+\Delta t]$. The (specific) catch ratio for a discrete time step is redefined as:

$$\eta_d(d,t_j) = \frac{\int_{t_j}^{t_j+\Delta t} R_{wdr}(d,t)\,dt}{\int_{t_j}^{t_j+\Delta t} R_h(d,t)\,dt} = \frac{S_{wdr}(d,t_j)}{S_h(d,t_j)} \quad ; \quad \eta(t_j) = \frac{\int_{t_j}^{t_j+\Delta t} R_{wdr}(t)\,dt}{\int_{t_j}^{t_j+\Delta t} R_h(t)\,dt} = \frac{S_{wdr}(t_j)}{S_h(t_j)} \tag{2}$$

where $S_{wdr}(d,t_j)$ and $S_h(d,t_j)$ are the specific WDR amount on the building and the specific unobstructed horizontal rainfall amount during time step $[t_j, t_j+\Delta t]$ for raindrops with diameter d. $S_{wdr}(t_j)$ and $S_h(t_j)$ respectively refer to the same quantities integrated over all raindrop diameters.

The catch ratio η is a complicated function of space and time. The six basic influencing parameters for η as defined in Eq. (2) are: (1) the building geometry (including environment topology), (2) the position on the building facade, (3) the reference wind speed, (4) the reference wind direction, (5) the horizontal rainfall intensity and (6) the horizontal raindrop-size distribution. In reality, the turbulent dispersion of raindrops is an additional parameter. It is often neglected, as will be done in this paper. This decision is based on the findings by Choi [13], by Blocken and Carmeliet [11] and on a review of the literature [1]. The reference wind speed U_{10} (m/s) refers to the horizontal component of the wind-velocity vector at 10 m height in the upstream undisturbed flow. The reference wind direction φ_{10} (degrees from north) refers to the direction of the reference wind speed. The horizontal raindrop-size distribution $f_h(d)$ (m^{-1}) refers to the raindrop-size distribution as a flux through a horizontal plane.

3. Measurement set-up

The design and installation of the measurement set-up have been described in detail in an earlier publication [5]. Only the headlines will be repeated here. The building under study is the VLIET test building of the Laboratory of Building Physics, Katholieke Universiteit Leuven, in Flanders, Belgium. It consists of two main modules, the flat-roof module and the sloped-roof module (Fig. 1). In between the main modules, there is a small terrace module. The building is 25.2 m long and 7.2 m wide. The height of the flat-roof module and the sloped-roof module is 4.3 m and 7.9 m respectively. The terrace height is 3.95 m. Roof overhang varies along the length of the building as indicated in Fig. 1. A view of the terrain situated south-west of the test building is provided in Fig. 2. The elements providing shielding from wind in the direct vicinity of the building are some low agricultural constructions to the south (which are situated about 80 m in front of the south-west facade) and a row of high poplars to the west side. The trees are about 50 to 60 m high and they are positioned along a straight line. The row of trees is situated closest to the sloped-roof-module corner. The distance between this corner and the trees, measured in south-west direction, is about 70 m, while the distance between the middle of the south-west facade and the row of trees, measured in south-west direction, is about 130 m. Further upstream (i.e. south-west), concentrations of mainly low-rise buildings are located (not visible in Fig. 2). The measurement set-up consists of (1) a meteorological mast positioned in front of the south-west facade that is equipped with three cup anemometers and one ultrasonic anemometer (Fig. 3), (2) a capacitance rain gauge placed inside a semi-circular turf wall (Fig. 3) and (3) a large number of WDR gauges (0.2x0.2m² catch area), mainly spread across the south-west facade because S-W is the prevailing wind direction in Flanders (Fig. 1). The wind-speed profile measured by the meteorological mast for south-west wind corresponds to a power law with exponent $\alpha = 0.176$ [5]. The reference wind speed U_{10} and the reference wind direction (both measured by the ultrasonic anemometer on top of the mast) and the horizontal rainfall intensity are obtained on a 1-minute basis.

4. Extended numerical wind-driven rain model

The extended numerical model for the assessment of the spatial and temporal distribution of WDR on buildings consists of five steps [11]:

1. The steady-state wind-flow pattern around the building is calculated using a CFD code.
2. Raindrop trajectories are obtained by injecting raindrops of different sizes in the calculated wind-flow pattern and by solving their equations of motion.
3. The specific catch ratio is determined based on the configuration of the calculated raindrop trajectories.
4. The catch ratio is calculated from the specific catch ratio and from the raindrop-size distribution. Catch-ratio charts are constructed for different zones (positions) on the building facade.
5. The experimental data record of reference wind speed, wind direction and horizontal rainfall intensity for a given rain event is combined with the appropriate catch-ratio charts to determine the corresponding spatial and temporal distribution of WDR on the building facade.

The steady-state wind-flow pattern is obtained by solving the Reynolds-Averaged Navier-Stokes (RANS) equations, usually in combination with one of the k-ε turbulence models. The equation of motion of a raindrop, moving in a wind-flow field characterized by a mean velocity vector $\vec{V}$ is:

$$\left(\frac{\rho_w - \rho}{\rho_w}\right)\vec{g} + \frac{3\mu}{\rho_w d^2}\cdot\frac{C_d Re_R}{4}\cdot\left(\vec{V} - \frac{d\vec{r}}{dt}\right) = \frac{d^2\vec{r}}{dt^2} \tag{3}$$

where Re_R is the relative Reynolds number (referring to the airflow around the raindrop):

$$Re_R = \frac{\rho d}{\mu}\left\|\vec{V} - \frac{d\vec{r}}{dt}\right\| \tag{4}$$

and ρ_w is the density of the raindrop, ρ the density of the air, g the gravitational acceleration, μ the dynamic air viscosity, d the raindrop diameter, C_d the raindrop drag coefficient, $\vec{r}$ the position vector of the raindrop in the xyz-space and t the time co-ordinate. The calculation of the specific catch ratio (η_d) and the catch ratio (η) is performed for a number of zones on the building facade (e.g. zone A_f in Fig. 4). For each zone, the same procedure is employed. In the steady-state wind-flow pattern – thus neglecting the turbulent dispersion of raindrops – raindrop trajectories of diameter d ending on the corner points of the zone form a stream tube (Fig. 4). Conservation of mass for the raindrops in the stream tube allows η_d to be expressed in terms of areas:

$$\eta_d(d) = \frac{R_{wdr}(d)}{R_h(d)} = \frac{A_h(d)}{A_f} \quad (5)$$

where A_f is the area of the zone on the building facade where η_d is to be determined and $A_h(d)$ is the area of the horizontal plane bounded by the injection positions of the raindrops of diameter d that end on the corner points of A_f. This plane $A_h(d)$ is located at a certain height in the undisturbed wind-flow pattern. Its location must allow the raindrops injected at that position to reach their terminal velocity of fall (vertical) and the wind velocity (horizontal) before entering the flow pattern that is disturbed by the presence of the building. The catch ratio η for a zone is obtained by multiplying η_d for each raindrop diameter d for this zone with the fraction of these drops in the spell (horizontal raindrop-size distribution $f_h(d)$) and by integrating over all raindrop diameters:

$$\eta = \int_d f_h(d)\,\eta_d(d)\,d\,d \quad (6)$$

It is important to note that for describing raindrop-size distributions, a probability-density function f(d) is usually provided that refers to the distribution of raindrops in a volume of air. For use in the present model however, where we deal with fluxes, the raindrop-size distribution f(d) applying to a volume of air has to be converted to the raindrop-size distribution as a flux through a horizontal plane $f_h(d)$; i.e. the horizontal raindrop-size distribution. The reason is that, due to the variation of the terminal velocity of fall V_t of a raindrop with size, the raindrop-size distribution in the air differs from the raindrop-size distribution through a horizontal plane. The former can be converted to the latter by multiplying with the raindrop terminal velocity of fall, as described in [1, 11]. The catch ratio η for a given zone (position) on the building facade is typically presented in a catch-ratio chart giving η as a function of the reference wind speed U_{10} and the horizontal rainfall intensity R_h for a given wind direction (Fig. 5). To determine the WDR amount on the building facade, the catch-ratio charts are combined with meteorological data records of the reference wind speed, the reference wind direction and the horizontal rainfall intensity. This procedure comprises partitioning the rain event into a number of equidistant time steps (e.g. 10-minute intervals). Each time step is considered steady-state and the meteorological data for each time step are used to extract the corresponding catch ratio from the appropriate catch-ratio chart. An essential part of this assessment model is using time-representative meteorological data. It has been shown that the use of 1-hour data (for 1-hour time steps) can yield significant underestimations of the calculated WDR amounts and therefore the use of data on – at least – a 10-minute basis is required [14].

5. Numerical modelling of the wind-flow pattern

The wind-flow pattern around the VLIET test building is modelled with the commercial CFD code Fluent 5.4 as a basis for modelling WDR in section 6. The study is focused on south-west wind. Three aspects require specific attention: (1) the choice of the turbulence model and wall functions, (2) the modelling of the approach-flow wind-speed profile and (3) the construction of the computational grid.

5.1. Choice of the turbulence model and wall functions

The purpose of the wind-flow simulations around the VLIET building is to model the behaviour of raindrops that impinge on the windward (south-west) facade. As a result, our interest is (mainly) in the wind-flow field upstream of the building. A recent validation study [15] of wind flow upstream of a cubic building model, using a tetrahedral computational grid, has indicated that the combination "realizable k-ε model [16], standard wall functions [17]" yields better results than other combinations including the standard k-ε model and non-equilibrium wall functions. Therefore, this combination will be applied in the present simulations. Note that the standard wall functions used in the model are modified for roughness effects based on the formulae by Cebeci and Bradshaw [18,19].

5.2. Modelling the approach-flow profile

The approach-flow profile (power law with exponent $\alpha = 0.176$) is measured at a distance of 20 m in front of the south-west facade (Fig. 3). In the CFD simulation, it is assumed that this profile represents the approach flow over the entire width of the computational domain. Given the complexity of the surroundings upstream of the facade (Fig. 2), this will in reality not be the case. Especially the row of trees, situated west of the building, is expected to have some influence. As can be seen in Fig. 2, the row of trees is situated closest to the sloped-roof-module corner. It is expected that the trees will somewhat slow down the approach-flow wind speed and this

effect will be more pronounced for the west corner of the building (sloped-roof module) than for the south corner (flat-roof module). We will focus on the consequences of this assumption in section 6.

5.3. Construction of the computational grid

The VLIET test building is characterized by important details (e.g. roof overhang) with small length scales. This necessitates the use of a high mesh resolution in these regions. On the other hand, near the top of the computational domain, cells can be relatively large. To be able to model details such as the roof overhang and to avoid using too much cells, an unstructured tetrahedral grid has been used. Three different grids have been made by refining the cells of the coarsest (initial) grid by about a factor $\sqrt{2}$. Some of the grid characteristics are given in Table 1. The characteristics of the CFD simulation (for Grid3) are listed in Table 2. The results of the grid-convergence study are displayed in Fig. 6 as wind-speed ratios along two horizontal lines A and B at a height of 4 m (top of the facade) that can be considered to be representative for part of the region that will be traversed by the raindrops before impinging on the south-west facade. No large differences between the solutions on the different grids can be observed. This is probably due to the fact that in all grids the control volumes have been clustered quite densely around the building. Because Fig. 6b and c show some (minor) differences between the results, Grid3 (finest grid) has been used for further study. Part of the surface grid is illustrated in Fig. 7a.

To avoid the use of excessively large cells near the ground [19], the ground roughness K_S in the Fluent 5.4 code has been taken equal to the aerodynamic roughness length $y_0 = 0.03$ m (see Table 2) and in order to achieve horizontal homogeneity of the approach-flow mean wind-speed profile in this situation, the inlet turbulent kinetic energy had to be reduced from $3.33(u^*_{ABL})^2$ to $1.5(u^*_{ABL})^2$, where u^*_{ABL} is the friction velocity associated with the simulation inlet profiles. More information on this matter is provided in [19]. It is important to note that calculation results of the wind-flow pattern in front of single buildings obtained this way have been successfully validated [15] illustrating the adequacy of this adjustment for the current WDR studies.

5.4. Results

Fig. 7b displays wind-speed contours (magnitude of 3D velocity vector divided by U_{10}) in a horizontal plane at (y = 3 m) height. The wind-flow pattern in front of the building is now briefly discussed based on Fig. 6:

1. Fig. 6b. The streamwise velocity component U is considerably reduced when approaching the building. The reduction is most pronounced in front of the sloped-roof module (which provides the largest obstruction for the wind flow; wind blocking) and least pronounced for the terrace module. The latter observation is caused by the location of the horizontal line: at 4 m height while the terrace module is only 3.95 m high. On the other hand, the wind speed near the building corners clearly increases from curve A to curve B.
2. Fig. 6c. Close to the building, the upward (vertical) velocity component strongly increases. At 4 m height, this effect is most pronounced for the flat-roof module and the terrace module that have a height of about 4 m. The sloped-roof module is much higher (7.9 m). Therefore, the line at 4 m height is situated close to the stagnation point of this module (low vertical wind speed).
3. Fig. 6d illustrates the dimensionless lateral velocity component. In general (line A), the flow approaching the sloped-roof module is deviated to the negative z-direction and vice versa for the flow approaching the other modules. Close to the building (line B), a quite irregular and peaked profile is observed. The location of the first (downward) peak corresponds to the location of the sloped-roof module edge, where the flow is strongly deviated in the negative z-direction. The location of the second peak corresponds to the location where the sloped roof ends and the terrace module begins. At this location, the approaching flow is deflected by the sloped roof towards the terrace module and sweeps over the terrace (in positive z-direction). The third peak is located at the flat-roof module edge, where the flow is again strongly deviated in the positive z-direction.

In the next section, it will be shown that this particular wind-flow pattern is responsible for the complex WDR distribution patterns on the building facade.

6. Numerical modelling of wind-driven rain and validation

6.1. Raindrop trajectories

The wind-flow pattern has been calculated for a reference wind speed $U_{10} = 10$ m/s. The wind-flow patterns for other reference wind-speed values (1-10 m/s in steps of 1 m/s) are obtained by linear scaling, which is allowed for bluff bodies with sharp edges. In each of the 10 wind-flow patterns, 3D Lagrangian particle tracking is performed for raindrops with diameters ranging from 0.3 to 1 mm in steps of 0.1 mm and from 1 to 6 mm in steps of 0.2 mm. The water density ρ_w used in the calculations is 1000 kg/m³. The drag coefficients C_d and the raindrop terminal velocities V_t are obtained from the experimental data from Gunn and Kinzer [20]. The

integration procedure for Eq. (3) is performed in a piecewise analytical manner with a maximum travel distance (length step) of each raindrop of $\Delta \ell = 0.05$ m.

6.2. Specific catch ratio

The specific catch ratio η_d has been calculated using two different procedures. The first procedure consists of selecting a number of rectangular zones (areas) on the building facade. The trajectories that end at the corner points of these areas are determined iteratively. By employing Eq. (5), the corresponding value for η_d is obtained for those specific areas. The second procedure consists of injecting a large number of raindrops from a dense, rectangular, horizontal injection grid in such a way that the entire south-west facade is covered with drops. Each set of three nearby raindrop trajectories that reach the facade is a separate (triangular) stream tube that marks a triangular area on the facade. The η_d–value for this area is attributed to the centre of gravity of the triangle. This way, values for η_d at a large number of data points scattered across the facade are obtained. Next, the data are interpolated on a fine rectangular grid on the facade to obtain η_d-values at each requested position. A distinction is made between both procedures because of the following reasons: (1) The first procedure is used for validation purposes. The areas are chosen to coincide with the collection areas of the WDR gauges. This allows determining exactly the values for η_d that correspond to the catch areas of the WDR gauges. This is especially important to get accurate results at those positions of the facade where large wetting gradients exist (e.g. below roof overhang) and where the second procedure (with interpolation) will provide somewhat less accurate results. (2) The second procedure is employed to provide an overall view of the distribution of η_d across the facade, because this procedure is less time-consuming than the first procedure. Employing these two procedures, η_d is calculated for all 33 raindrop diameters and for each reference wind-speed value. It has been determined for the collection areas of all WDR gauges at the facade using the first procedure and for the entire south-west facade using the second procedure. Fig. 8 illustrates the application of the first procedure for the VLIET building. The raindrop trajectories that are displayed are the result of the iterative procedure. The calculation has been performed in such a way that trajectory endpoints are situated within a distance of 0.001 m from the corner points of the collection areas of the WDR gauges.

6.3. Catch ratio

Adopting the raindrop-size distribution according to Best [21], the catch ratio η is determined for all positions at the south-west facade and for south-west wind direction as a function of the reference wind speed and the horizontal rainfall intensity using Eq. (6). The integration procedure for Eq. (6) is performed discretely, using the midpoint rule to integrate over the 33 raindrop diameters. Fig. 9 illustrates the catch-ratio charts for position 19 and 20 on the south-west facade.

Two important remarks have to be made concerning the configuration of the building model used in the simulations: (1) The test facade of the flat-roof module that contains the gauges 13-15 is protruded (0.02 m) compared to the others [5]. This protrusion, which corresponds to a reduction in roof overhang length, has not been modelled. As a result, the numerical model will provide slightly lower WDR amounts at these gauge positions than in reality. (2) In reality, there are two condensers on the roof of the terrace module (see [5]: Fig. 3b and 9e). These condensers have not been included in the building model. This will not influence the WDR catch by the gauges, except for gauges 19 and 20 that are positioned just below the condensers. The influence of the presence of the condensers on the WDR catch is due to the wind-blocking effect, which refers to the upstream slow-down of the approaching wind (wind-blocking) by these obstacles [22]. This influence has been assessed using simplified 2D modelling. Figs. 10a-b illustrate the configuration of the 2D models of the terrace module. The entire procedure (modelling of wind-flow pattern, raindrop trajectories, specific catch ratio and catch ratio) has been conducted for the two 2D configurations, for the position indicated by the black rectangle in Figs. 10a-b (i.e. the position of the WDR gauges number 19 and 20). The resulting η-charts are given in Figs. 10c-d. Note that at these positions, the surfaces $\eta = f(U_{10},R_h)$ are almost plane surfaces with a small inclination along the R_h-axis (except for the lightest horizontal rainfall intensities for which the inclination is very steep). The ratio of the inclinations along the U_{10}-axis of both figures is about 0.85. Therefore it can be stated that, in 2D, neglecting the presence of the condensers yields an overestimation of η (and hence of the WDR amount) of about 18%. It is recognized that 2D modelling can significantly deviate from 3D reality. Fig. 6d and Fig. 8 clearly illustrate the 3D character of the wind-flow pattern and the raindrop trajectories at this location. On the other hand, Figs. 9a-b illustrates the η-charts that have been obtained by 3D modelling, for position 19 and 20 at the top of the terrace-module facade. Despite the 3D character of the situation, the η-charts in Figs. 9a-b and Fig. 10c are remarkably alike. This supports the assumption that also in 3D, the overestimation of η will be close to 18%. Therefore the 3D results at positions 19 and 20 have been corrected (reduced) by this amount.

6.4. Spatial and temporal distribution of wind-driven rain and validation

The extended numerical WDR simulation model is applied to determine the spatial and temporal distribution of wind-driven rain on the VLIET building for three different on-site recorded rain events that were selected from the experimental WDR dataset [5].

6.4.1. Rain event 1

The rain event is given in Fig. 11a (02-05/02/2002). It is a cumuliform rain event that is composed of a few rain showers, the most intensive of which occur at the end of the rain event. The total horizontal rainfall amount S_h = 15.7 mm. The wind direction during rain is approximately south-west (225°). Fig. 11b shows a good agreement between the calculated and the measured temporal distribution of WDR at gauge position 13. The absolute WDR measurement error is estimated following the procedure outlined in [4,5]: error E_{wdr} = 0.8 mm. Note however that the 0.02 m protrusion of this facade part has been neglected in the numerical model. The spatial distribution for the rain event is given in Fig. 12 (ratio of total WDR amount S_{wdr} for the rain event divided by total horizontal rainfall amount S_h = 15.7 mm). Figs. 12a-b illustrate the numerical results. Fig. 12b additionally shows the calculated values at the positions of the WDR gauges. Fig. 12c holds the measurement results. The WDR measurement error estimate for the ratio S_{wdr}/S_h is e_{wdr} = 0.05. Note that the contours in Figs. 12a-b have been determined without correcting for the presence of the condensers, while the values at the positions 19 and 20 (indicated within the square rectangles in Fig. 12b) have been corrected. The black areas indicate those parts of the facade that are sheltered from rain by the roof overhang. Generally, the agreement between numerical and experimental results is good. The numerical simulation provides a good indication of the very distinct wetting pattern across the facade, with the flat-roof module building facade receiving significantly more WDR than the sloped-roof module facade, to a large extent due to the wind-blocking effect that is larger for the sloped-roof module [22]. However, some overestimations by the numerical model are noted. Large discrepancies (overestimations) are present at the sloped-roof-module corner (positions 2-3). This can – at least partly – be explained by the retarding effect by the row of trees on the wind flow (which is not included in the model but which is present in reality).

The distinct wetting pattern is directly related to the features of the wind-flow pattern that were shown in Fig. 6. The high vertical wind-speed components in Fig. 6c are responsible for the high catch ratios at the top edge of the terrace module and the flat-roof module, despite the presence of the roof overhang, while the catch-ratio values at the top of the sloped-roof module are quite low. The peak values in the lateral wind speed in Fig. 6d are directly responsible for the high catch ratios at the outer vertical edges of the sloped-roof module and the flat-roof module.

6.4.2. Rain event 2

The rain event is illustrated in Fig. 13a (05-08/02/2002). It is a cumuliform rain event that is mainly composed of two rain showers, one with heavy and one with moderate rainfall intensity. The total horizontal rainfall amount S_h = 11.3 mm. The wind direction during rain is approximately south-west (225°). Fig. 11b shows a good agreement between the calculated and measured temporal distribution at gauge position 13. The estimated measurement error E_{wdr} = 0.6 mm. The spatial distribution for the rain event is given in Fig. 14. The estimated measurement error for the ratio S_{wdr}/S_h is e_{wdr} = 0.05. Again, the agreement between numerical and experimental results is generally good. Large discrepancies are found near the sloped-roof module corner (positions 2-3) due to the retarding effect by the row of trees on the wind flow. Note that at position 1, a good agreement is found instead of an overestimation. This is attributed to errors caused by the fact that this position is situated in the transition region between the wet and the dry part of the facade. This region is caused by the shelter by the roof overhang. In this region, due the large wetting gradients, it is more difficult to predict the WDR distribution accurately.

6.4.3. Rain event 3

Finally, the numerical results for a long, stratiform rain event (25-26/02/2002) (Fig. 15a) are presented. The total horizontal rainfall amount S_h = 26.7 mm. The wind direction during rain is approximately south-west (225°). This is the rain event – among all rain events included in the validation study, see section 6.4.4 – for which the least agreement between the numerical and the experimental results has been obtained. Fig. 15b displays the calculated and measured temporal distribution at gauge position 14 during the stratiform rain event. The estimated measurement error e_{wdr} = 0.5 mm. Although the relative temporal variation is predicted fairly well, the WDR amount is underestimated by the numerical model, which is partly due to the 0.02 m protrusion of this facade part. Fig. 16 shows the spatial distribution. The estimated measurement error for the ratio S_{wdr}/S_h is e_{wdr} = 0.02. Although the general agreement is still acceptable, significant overestimations are noted, which are most pronounced for – but not restricted to – the positions near the sloped-roof-module corner.

6.4.4. Other rain events

Validation for the other rain events comprised in the experimental WDR dataset [5] can be found on the website of the Laboratory of Building Physics, Katholieke Universiteit Leuven. The website supplements the information presented in this paper: www.kuleuven.be/bwf/projects/WDRCFDvalidation

7. Discussion

The discussion focuses on the accuracy of the WDR measurements, on the accuracy of the numerical simulations, on the current validation results and on future validation efforts.

7.1. Accuracy of the wind-driven rain measurements

In selecting the experimental WDR data for CFD validation, the guidelines for minimizing errors have been carefully adhered to [4,5]. Wind errors have been limited by considering only rain events with wind directions that were approximately perpendicular to the facade under study. Evaporative losses from the reservoirs have been measured and the measurements have been corrected for this error. Given the low wind-speed values for all rain events, the influence of splashing is negligible [4]. As a result, the estimated adhesion-water-evaporation error [4] that has been mentioned for every rain event in section 6 is an adequate and conservative estimate of the maximum WDR measurement error.

7.2. Accuracy of the numerical simulations

The accuracy of the numerical simulations is determined by the accuracy of the calculated wind-flow pattern, by the accuracy of the calculated raindrop trajectories (and thus the catch ratio) and by the accuracy of the meteorological input data (reference wind speed, wind direction, horizontal rainfall intensity).

Care has been taken in modelling the wind-flow pattern around the building. The approach-flow wind-speed profile has been measured on site and this measured profile has been used as input for the simulations. Although the wind-speed profile was measured downstream of the row of trees, the laterally-different retarding effect caused by these trees to the flow (larger for the sloped-roof module corner than for the rest of the building) appears to be important. This effect has been found systematically for all rain events by comparing WDR calculations and measurements.

Two assumptions have been made in the WDR model, that are considered to be important by WDR researchers: adopting the raindrop-size distribution according to Best [21] and neglecting the turbulent dispersion of raindrops. Although the raindrop-size distribution of Best is based on an extensive study for a large number of rain events, deviations from the prescribed spectra will have occurred. However, earlier studies [11,23] have provided indications that the sensitivity to raindrop-size spectra is rather small and that the knowledge of the exact raindrop-size distribution might not be that important. A tentative conclusion is that this statement is corroborated by the validation study in this paper: in spite of the very different rain events that have been modelled, using the size distribution by Best [21], a systematically satisfactory agreement (also with remarkably systematic discrepancies) has been found. If deviations in raindrop-size spectra were important, one would expect a less systematic behaviour from the different rain events. Turbulent dispersion has deliberately not been included in the numerical model. There are two reasons for this, the first of which is a practical reason and the second of which has more fundamental grounds: (1) Turbulent dispersion does not allow the determination of the specific catch ratio by the use of stream tubes, as the raindrop trajectories are now highly variable in time. Less effective and more time-consuming techniques (much more raindrop trajectories) will be needed to obtain adequate results. (2) Turbulent dispersion is typically modelled by extracting the turbulent kinetic energy from the wind-flow simulation and by using these values as a measure to add random fluctuations to the wind-velocity components that appear in the raindrop's equation of motion (Eq. 3). The wind-flow simulations are generally conducted using the RANS approach in combination with a turbulence model based on the isotropic eddy viscosity hypothesis. Most often, one of the versions of the k-ε is employed. These turbulence models, and in particular the k-ε turbulence model, fail to accurately reproduce the turbulent kinetic energy in front of buildings. As a result, it is clear that turbulent dispersion modelling should be conducted with extreme care and preferably with other turbulence models that take into account the anisotropy of the turbulent viscosity (e.g. Reynolds Stress Models or Large Eddy Simulation). On the other hand, the most detailed studies of WDR including turbulent dispersion have been conducted by Lakehal et al. [24] and by Choi [13]. Lakehal et al. indicated that turbulent dispersion is generally not important, except in unusual situations where the mean wind speed upstream of the facade is very small (e.g. in a narrow street canyon perpendicular to the approaching wind direction). Choi demonstrated that there can be a significant influence of e.g. 3s durations gusts on short-term WDR fluctuations but that turbulent dispersion has only a small effect on the mean WDR (i.e. at time scales above 10 minutes). The systematic character of both the agreement and the discrepancies between measurements

and simulations found in this paper for very different rain events seems to corroborate the findings of these authors.

The accuracy of the meteorological input data is determined by the accuracy of the reference wind-speed, wind-direction and horizontal-rainfall intensity measurements and by the sample size of the meteorological data. The latter issue is very important, as described in [14]. It has been taken into account in this study by the use of short-term wind and rain data (1-minute data converted to 10-minute data, instead of the commonly used 1-hour averages that can give rise to very large errors in the calculated WDR amounts).

7.3. Current validation results and future validation efforts

For all rain events, the same systematic WDR pattern but also the same systematic pattern of discrepancies (overestimations) has been found. The overestimation near the sloped-roof-module corner can – at least partly – be attributed to the retarding effect by the row of trees, causing lower experimental WDR values at these positions. This effect has not been included in the numerical model. The reason for the occurrence of the (other) systematically overestimated values by the numerical model is less clear. They may be attributed to a variety of causes: modelling errors in the wind-flow pattern around the building, the difficulty in modelling the sweeping effect of raindrops in combination with roof overhang, etc.

Future validation studies will benefit from additionally conducting wind-speed measurements around the buildings under study to allow validation of the calculated wind-flow pattern as well. Future validation studies should focus on at least three main topics: (1) WDR on different building configurations in different environment topologies; (2) WDR on building groups and the interaction of buildings on each others' WDR exposure; (3) the WDR distribution over various topographic features such as hills and valleys where buildings are constructed. As a first step in the latter topic, numerical simulations and validation of the WDR distribution over small-scale topographic features (ridges, hills, valleys) have recently been conducted, providing a good agreement with the corresponding full-scale measurements [25,26].

The general conclusion however is the current lack of detailed, accurate and reliable experimental WDR datasets. This is the most important obstruction towards additional CFD validation. The strict accuracy guidelines that have to be forced upon WDR datasets are an additional obstacle [4,5]. The construction of such datasets and their use for model validation is an important task for the future.

8. Conclusions

CFD simulations have been conducted to determine the spatial and temporal distribution of wind-driven rain on the facade of the low-rise VLIET test building. On-site measured meteorological data records of reference wind speed, reference wind direction and horizontal rainfall intensity have been used as input for the simulations. The numerical results have been validated by comparison with the corresponding full-scale wind-driven rain measurements, which were extracted from a high-resolution wind-driven rain dataset. In spite of the complexity of the building geometry (roof overhang, protruded and recessed facade parts), the complexity of the surroundings (low agricultural constructions, row of trees) and the inherent complexity of conducting CFD simulations, a satisfactory agreement has been obtained for a number of very different rain events, for the spatial as well as for the temporal WDR distribution. The main reason for the discrepancies that have been observed is believed to be the simplified modelling of the upstream terrain. In particular, the influence of the differential retarding effect of the row of trees has been made clear by the validation study.

Acknowledgements

This research was conducted while the first author was a post-doctoral research fellow of the FWO-Flanders that supports and stimulates fundamental research in Flanders (Belgium). Their contribution is gratefully acknowledged.

Nomenclature

A_f	area of a zone on the building facade (m²)
A_h	area of a horizontal surface at a certain height in the upstream undisturbed flow (m²)
C_d	raindrop drag coefficient
C_{Ks}	roughness constant in the standard wall function modified-for-roughness
$C_{2\varepsilon}$	constant in the realizable k-ε turbulence model
d	raindrop diameter (mm)
E	empirical constant for wall roughness in wall-function method
e_{wdr}	error estimate for the ratio S_{wdr}/S_h
f(d)	probability-density function of raindrop sizes in a volume of air (m^{-1})

$f_h(d)$	probability-density function of raindrop sizes falling through a horizontal plane (m^{-1})
j	index for time step
k	turbulent kinetic energy (m^2/s^2)
K_S	physical roughness height (m)
Re_R	relative Reynolds number
R_h	horizontal rainfall intensity, i.e. through a horizontal plane (L/m²h or mm/h)
R_{wdr}	wind-driven rain intensity (L/m²h or mm/h)
S_h	horizontal rainfall amount, i.e. through a horizontal plane (L/m² or mm)
S_{wdr}	wind-driven rain amount (L/m² or mm)
t	time (s)
u^*_{ABL}	friction velocity associated with the inlet profiles of U, k and ε (m/s)
U, V, W	streamwise, vertical and lateral component of the mean wind-velocity vector (m/s)
U_{10}	reference wind speed at 10 m height in the upstream undisturbed flow (m/s)
V_t	raindrop terminal velocity of fall (m/s)
x, z	streamwise and spanwise co-ordinate (m)
y	height co-ordinate (m)
y_0	aerodynamic roughness length (m)
y_P	distance from the centre point P of the wall-adjacent cell to the wall
α	power-law exponent
$\Delta\ell$	maximum length step in raindrop trajectory calculation (m)
ε	turbulence dissipation rate (m^2/s^3)
η_d	specific catch ratio
η	catch ratio
κ	von Karman constant (≈ 0.42)
μ	air dynamic viscosity (kg/ms)
ρ	air density (kg/m^3)
ρ_w	water density (kg/m^3)
σ_κ, σ_ε	turbulent Prandtl number for k, ε
φ_{10}	wind direction at 10 m height in the upstream undisturbed flow (degrees from north)
$\vec{V}$	mean wind-velocity vector (m/s)
$\vec{r}$	position vector of the raindrop in the xyz-space (m)
CFD	Computational Fluid Dynamics
CV	Control Volume
RANS	Reynolds-Averaged Navier Stokes
VLIET	Flemish Impulse Programme for Energy Technology
WDR	Wind-Driven Rain

References

[1] Blocken B, Carmeliet J. A review of wind-driven rain research in building science. Journal of Wind Engineering and Industrial Aerodynamics 2004;92(13): 1079-1130.

[2] Högberg AB, Kragh MK, van Mook, FJR. A comparison of driving rain measurements with different gauges. Proceedings of the 5th Symposium of Building Physics in the Nordic Countries, Gothenburg; 1999, p. 361-368.

[3] Van Mook FJR. Driving rain on building envelopes. Ph.D. thesis. Building Physics Group (FAGO), Technische Universiteit Eindhoven, Eindhoven University Press, Eindhoven, The Netherlands; 2002.

[4] Blocken B, Carmeliet J. On the accuracy of wind-driven rain measurements on buildings. Building and Environment 2006;41(12): 1798-1810.

[5] Blocken B, Carmeliet J. High-resolution wind-driven rain measurements on a low-rise building – experimental data for model development and model validation. Journal of Wind Engineering and Industrial Aerodynamics 2005;93(12): 905-928.

[6] Choi ECC. Numerical simulation of wind-driven rain falling onto a 2-D building. Asia Pacific Conference on Computational Mechanics, Hong Kong; 1991. p. 1721-1728.

[7] Choi ECC. Simulation of wind-driven rain around a building. Journal of Wind Engineering and Industrial Aerodynamics 1993;46&47: 721-729.

[8] Choi ECC. Determination of wind-driven rain intensity on building faces. Journal of Wind Engineering and Industrial Aerodynamics 1994;51: 55-69.
[9] van Mook F.J.R. Full-scale measurements and numeric simulations of driving rain on a building, 10ICWE, Copenhagen, Denmark, 21-24 June, 1999, pp. 1145-1152.
[10] Hangan H. Wind-driven rain studies. A C-FD-E approach. Journal of Wind Engineering and Industrial Aerodynamics1999;81: 323-331.
[11] Blocken B, Carmeliet J. Spatial and temporal distribution of driving rain on a low-rise building. Wind and Structures 2002;5(5): 441-462.
[12] Tang W, Davidson CI. Erosion of limestone building surfaces caused by wind-driven rain. 2. Numerical modelling. Atmospheric Environment 2004;38(33): 5601-5609.
[13] Choi ECC. Numerical modelling of gust effect on wind-driven rain. Journal of Wind Engineering and Industrial Aerodynamics 1997;72: 107-116.
[14] Blocken B, Carmeliet J. 2007. On the errors associated with the use of hourly data in wind-driven rain calculations on building facades. Atmospheric Environment 41(11): 2335-2343.
[15] Blocken B. 2004. Wind-driven rain on buildings: measurements, numerical modelling and applications. PhD thesis, Laboratory of Building Physics, Katholieke Universiteit Leuven.
[16] Shih TH, Liou WW, Shabbir A, Zhu J. A new k-ε eddy-viscosity model for high Reynolds number turbulent flows – model development and validation. Computers and Fluids 1995;24(3): 227-238.
[17] Launder BE, Spalding DB. The numerical computation of turbulent flows. Computer Methods in Applied Mechanics and Engineering 1974;3: 269-289.
[18] Cebeci T, Bradshaw P. Momentum transfer in boundary layers. Hemisphere Publishing Corporation, New York; 1977.
[19] Blocken B, Stathopoulos T, Carmeliet J. 2006. CFD simulation of the atmospheric boundary layer – wall function problems. Atmospheric Environment. Submitted.
[20] Gunn R, Kinzer GD. The terminal velocity of fall for water droplets in stagnant air. Journal of Meteorology 1949;6: 243-248.
[21] Best AC. The size distribution of raindrops. Quarterly Journal of the Royal Meteorological Society 1950;76: 16-36.
[22] Blocken B, Carmeliet J. The influence of the wind-blocking effect by a building on its wind-driven rain exposure. Journal of Wind Engineering and Industrial Aerodynamics 2005;94(2): 101-127
[23] Choi ECC. Parameters affecting the intensity of wind-driven rain on the front face of a building. Journal of Wind Engineering and Industrial Aerodynamics 1994;53: 1-17.
[24] Lakehal D, Mestayer PG, Edson JB, Anquetin S, Sini JF. Eulero-Lagrangian simulation of raindrop trajectories and impacts within the urban canopy. Atmospheric Environment 1995;29(23): 3501-3517.
[25] Blocken B, Carmeliet J, Poesen J. 2005. Numerical simulation of the wind-driven rainfall distribution over small-scale topography in space and time. Journal of Hydrology 2005;315(1-4): 252-273.
[26] Blocken B, Poesen J, Carmeliet J. 2006. Impact of wind on the spatial distribution of rain over micro-scale topography – numerical modelling and experimental verification. Hydrological Processes 2006;20(2): 345-368.

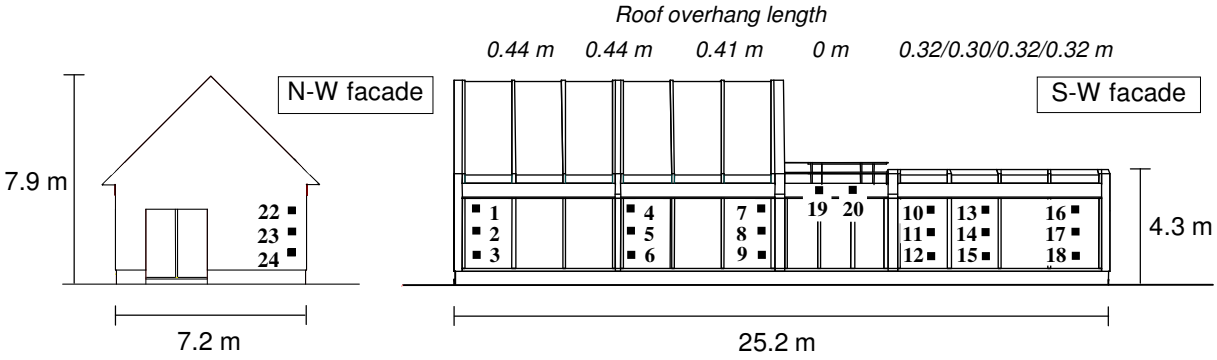

Fig. 1 VLIET test building. North-west and south-west facade. The building dimensions, including roof overhang length, and the positions and numbers of the wind-driven rain gauges (indicated by black squares) are indicated.

Fig. 2. View at the site south-west of the VLIET building. (Photograph taken with the back against the south-west facade).

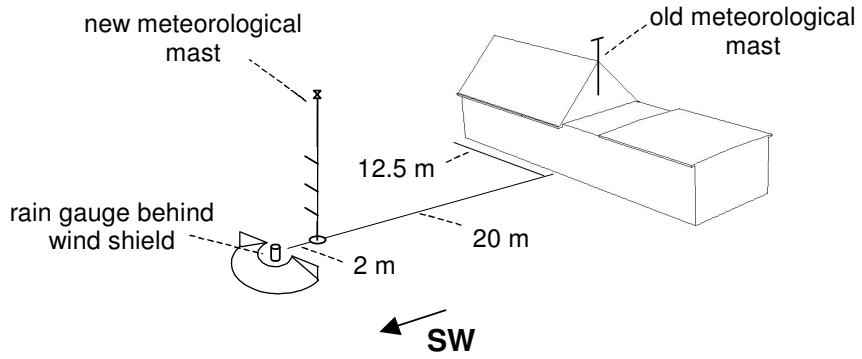

Fig. 3. Location of the (new) meteorological station (mast and horizontal rain gauge) in front of the south-west facade.

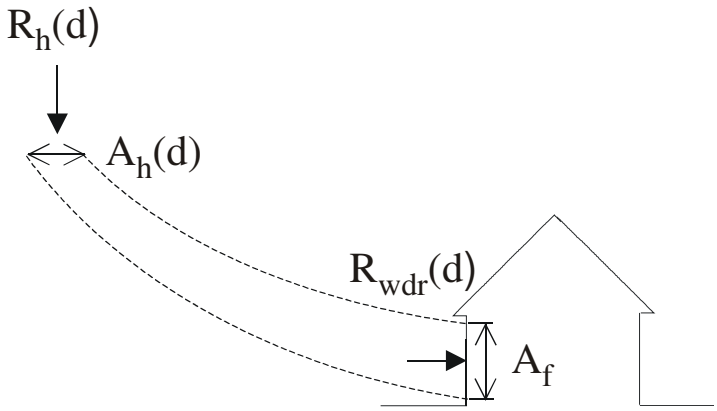

Fig. 4. Stream tube bounded by two raindrop trajectories. The specific catch ratio η_d for zone A_f and for raindrops with diameter d is determined based on conservation of mass for the raindrops in the stream tube.

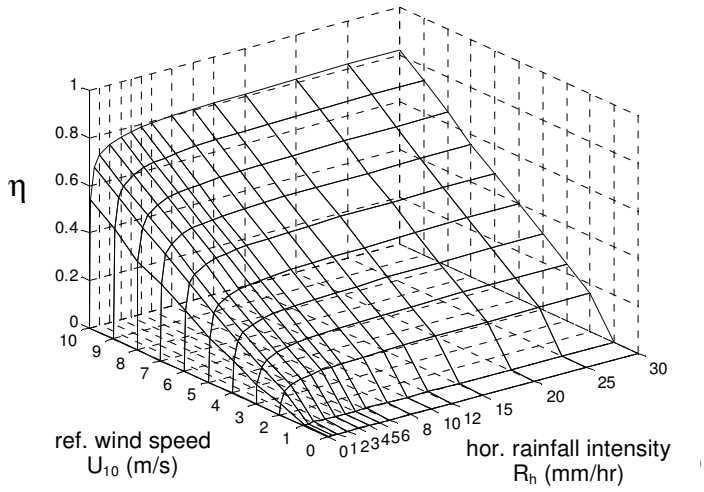

Fig. 5. Typical example of a catch-ratio chart or η-chart that presents the catch ratio as a function of the reference wind speed U_{10} and the horizontal rainfall intensity R_h, for a given position on the building facade and for a given wind direction.

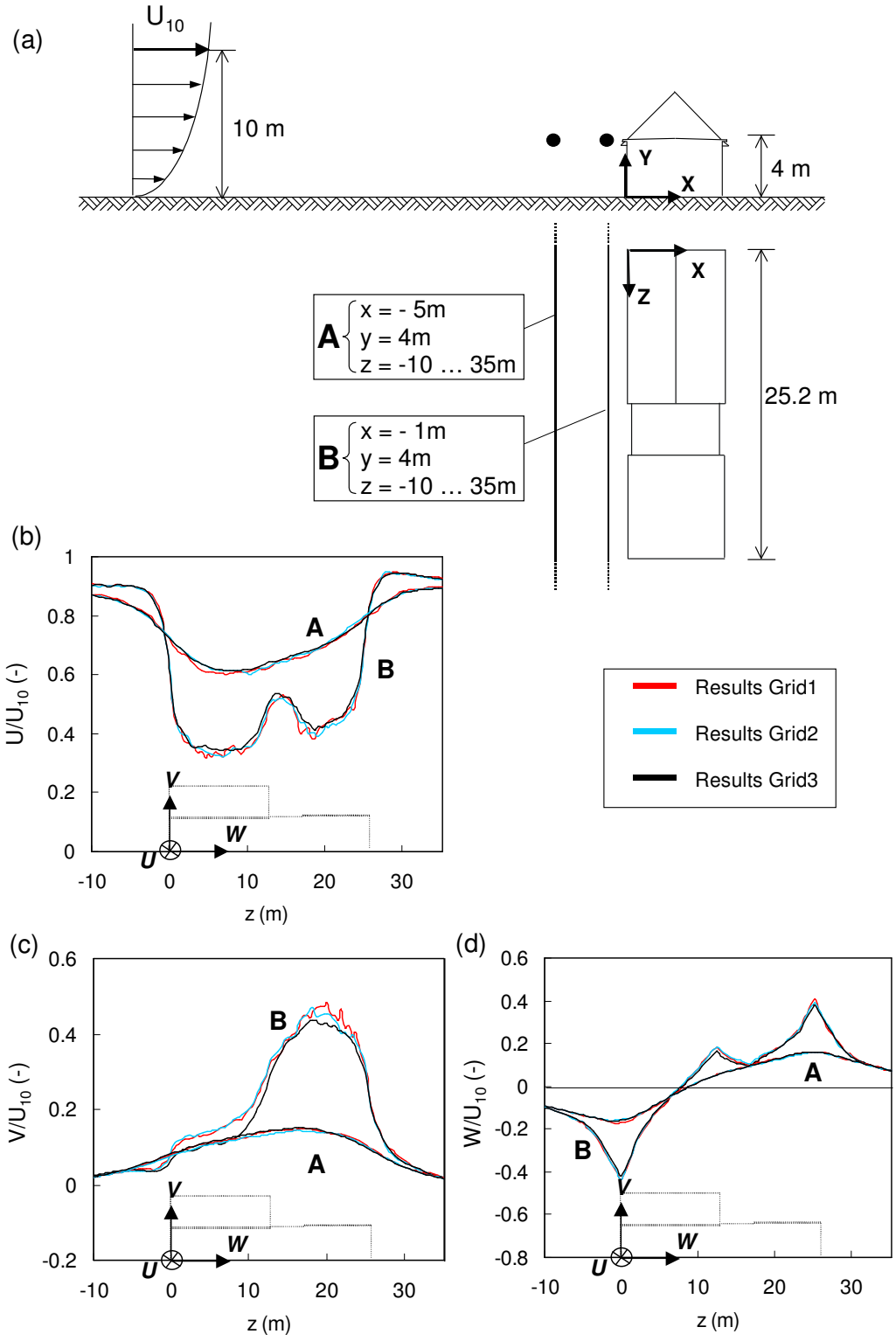

Fig. 6. Grid-convergence study for the grids given in Table 1. (a) Schematic illustration of the VLIET test building and the positions of the horizontal lines A and B along which the wind-speed profiles are plotted. (b) Dimensionless streamwise mean wind speed U/U_{10}. (c) Dimensionless vertical mean wind speed V/U_{10}. (d) Dimensionless lateral mean wind speed W/U_{10}.

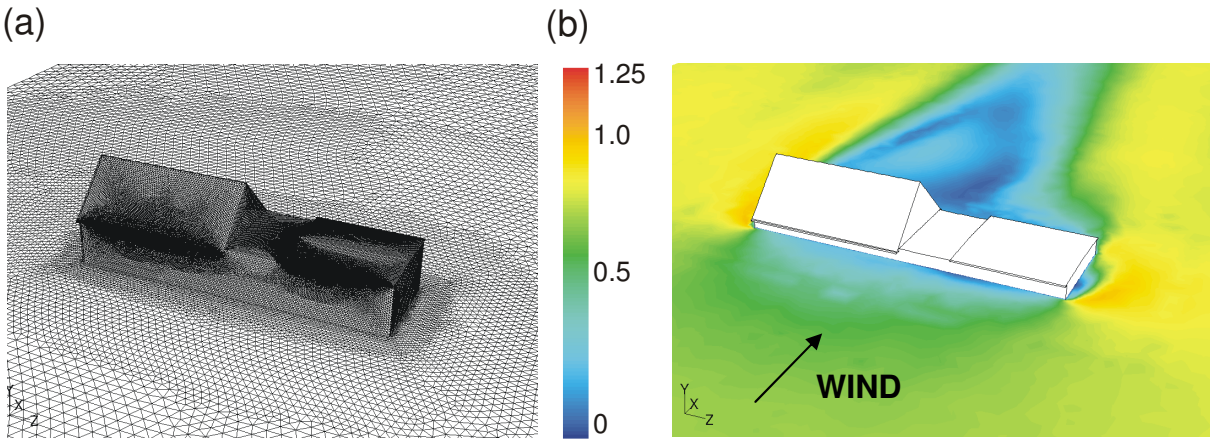

Fig. 7. (a) Unstructured, tetrahedral grid on the surface of the VLIET test building and on part of the ground surface around it (Grid R3: 1017518 cells). (b) Contours of the dimensionless wind speed (magnitude of the 3D velocity vector divided by U_{10}) in a horizontal plane at height y = 3 m above ground. The reference wind direction is perpendicular to the facade.

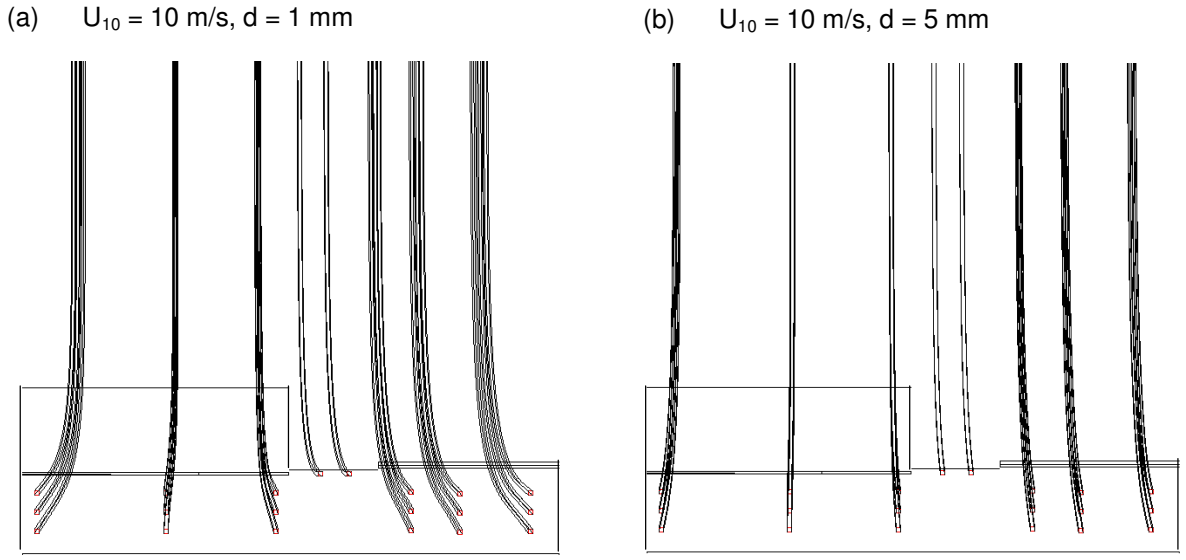

Fig. 8. Illustration of the raindrop trajectories that end on the corner points of 20 areas on the south-west facade of the VLIET building. The 20 areas coincide with the collection areas of the wind-driven rain gauges (see Fig. 1). (a) Reference wind speed U_{10} = 10 m/s, raindrop diameter d = 1 mm, (b) U_{10} = 10 m/s, d = 5 mm.

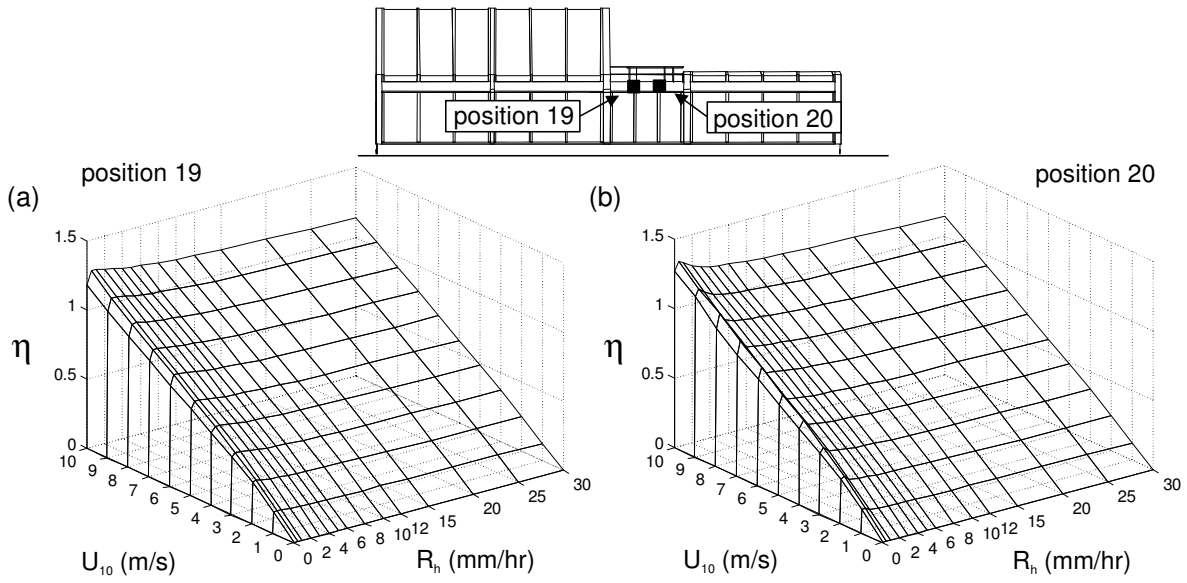

Fig. 9. Catch ratio η for position 19 and 20 as obtained from simulations with the 3D VLIET building model (without condenser on the roof).

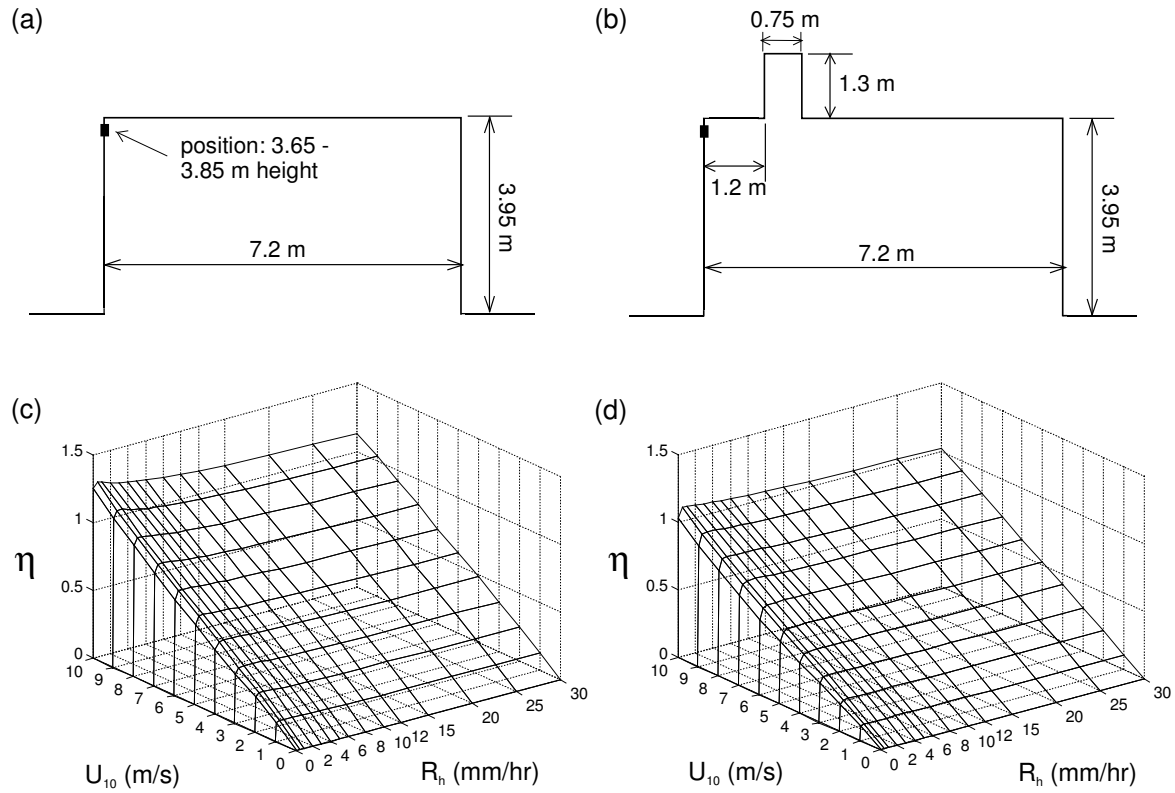

Fig. 10 (a-b) 2D model of the terrace module (a) without and (b) with condenser on the roof. The position at which the wind-driven rain gauges are installed is indicated by the black rectangle. (c-d) Catch ratio η as a function of reference wind speed U_{10} and horizontal rainfall intensity R_h for the position indicated and for (c) the 2D model without condenser on the roof and (d) the 2D model with condenser on the roof.

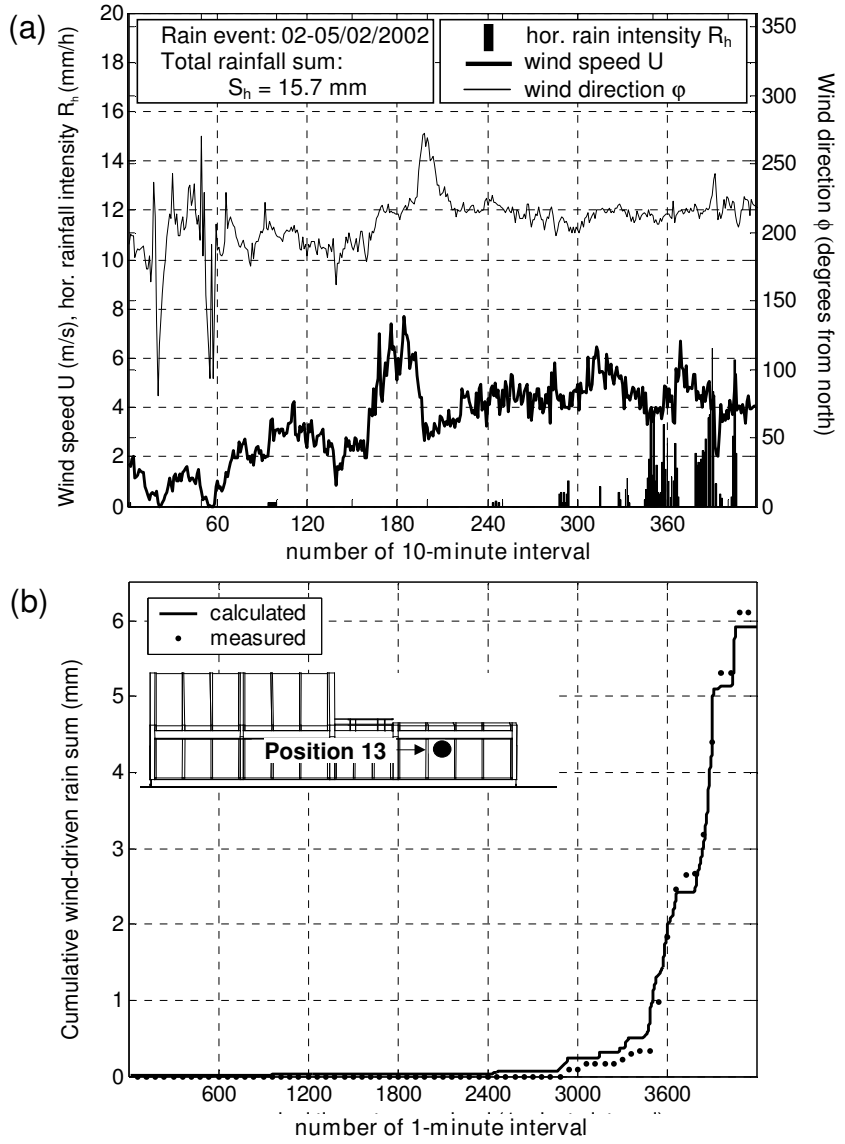

Fig. 11. (a) Meteorological data (reference wind speed, wind direction, horizontal rainfall intensity) measured during the rain event (02-05/02/2002). Total horizontal rainfall amount S_h = 15.7 mm. (b) Temporal distribution of the experimentally and numerically determined cumulative wind-driven rain amount at position 13 of the south-west facade.

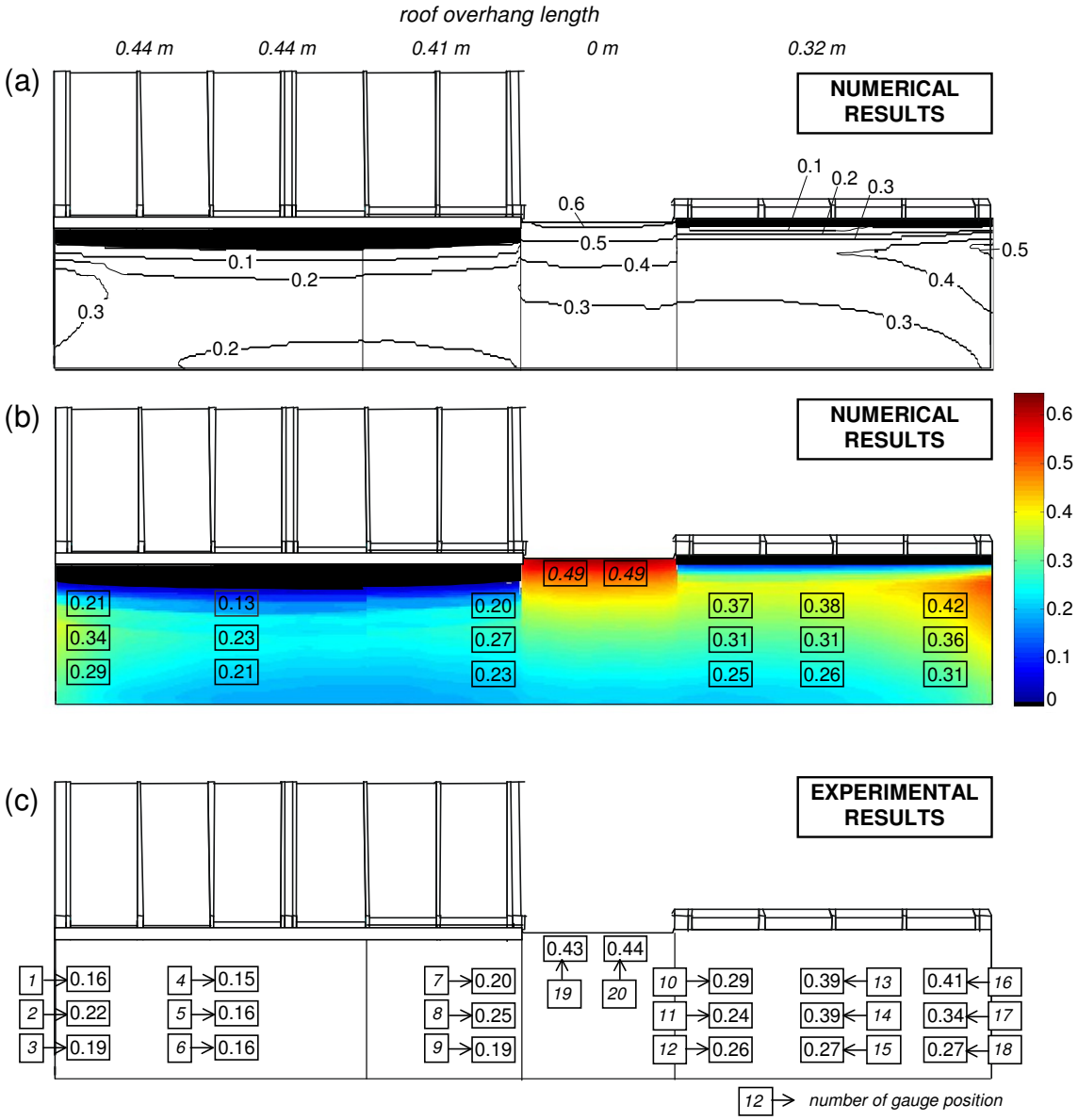

Fig. 12. Spatial distribution of the ratio S_{wdr}/S_h (total wind-driven rain amount to total horizontal rainfall amount) for the rain event (02-05/02/2002) (rain event is illustrated in Fig. 11a). The total horizontal rainfall amount S_h = 15.7 mm. (a-b) Numerical results. In Fig. 12b, the calculated ratios at the location of the wind-driven rain gauges are additionally indicated. (c) Experimental results.

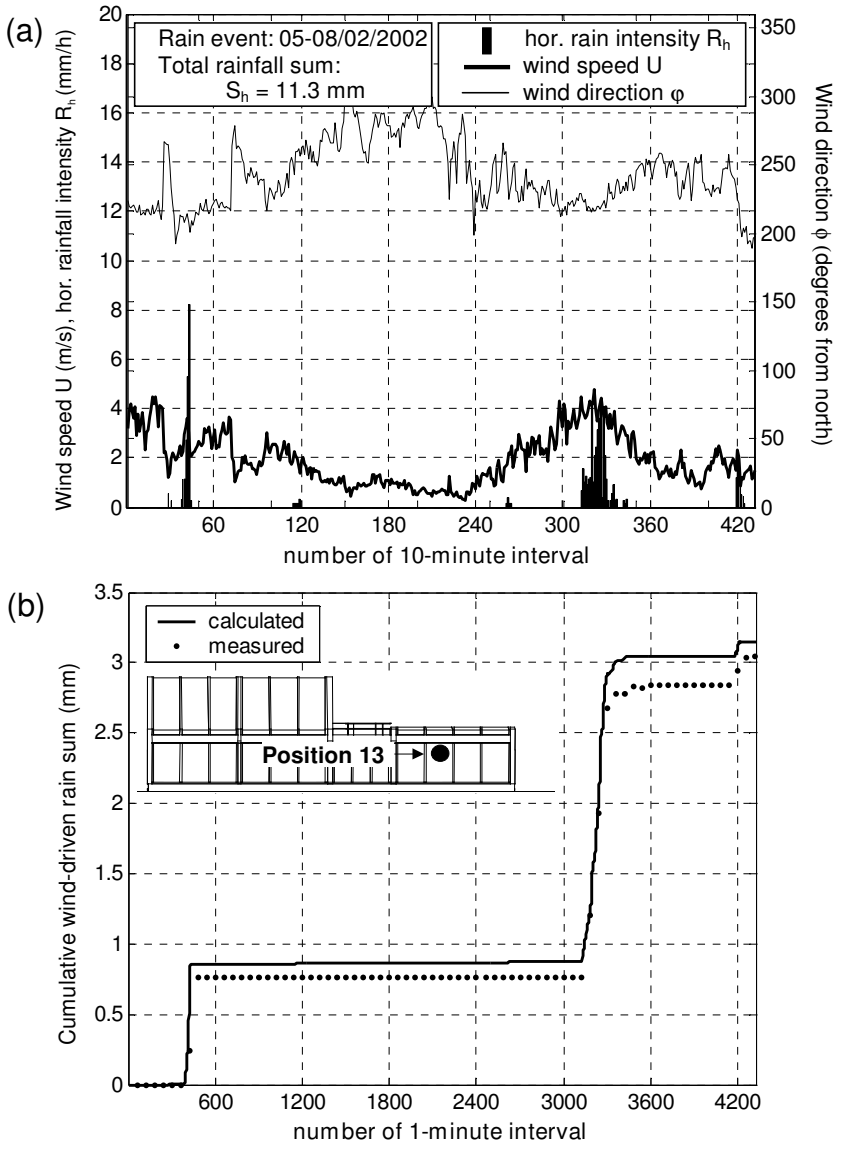

Fig. 13. (a) Meteorological data (reference wind speed, wind direction, horizontal rainfall intensity) measured during the rain event (05-08/02/2002). Total horizontal rainfall amount S_h = 11.3 mm. (b) Temporal distribution of the experimentally and numerically determined cumulative wind-driven rain amount at position 13 of the south-west facade.

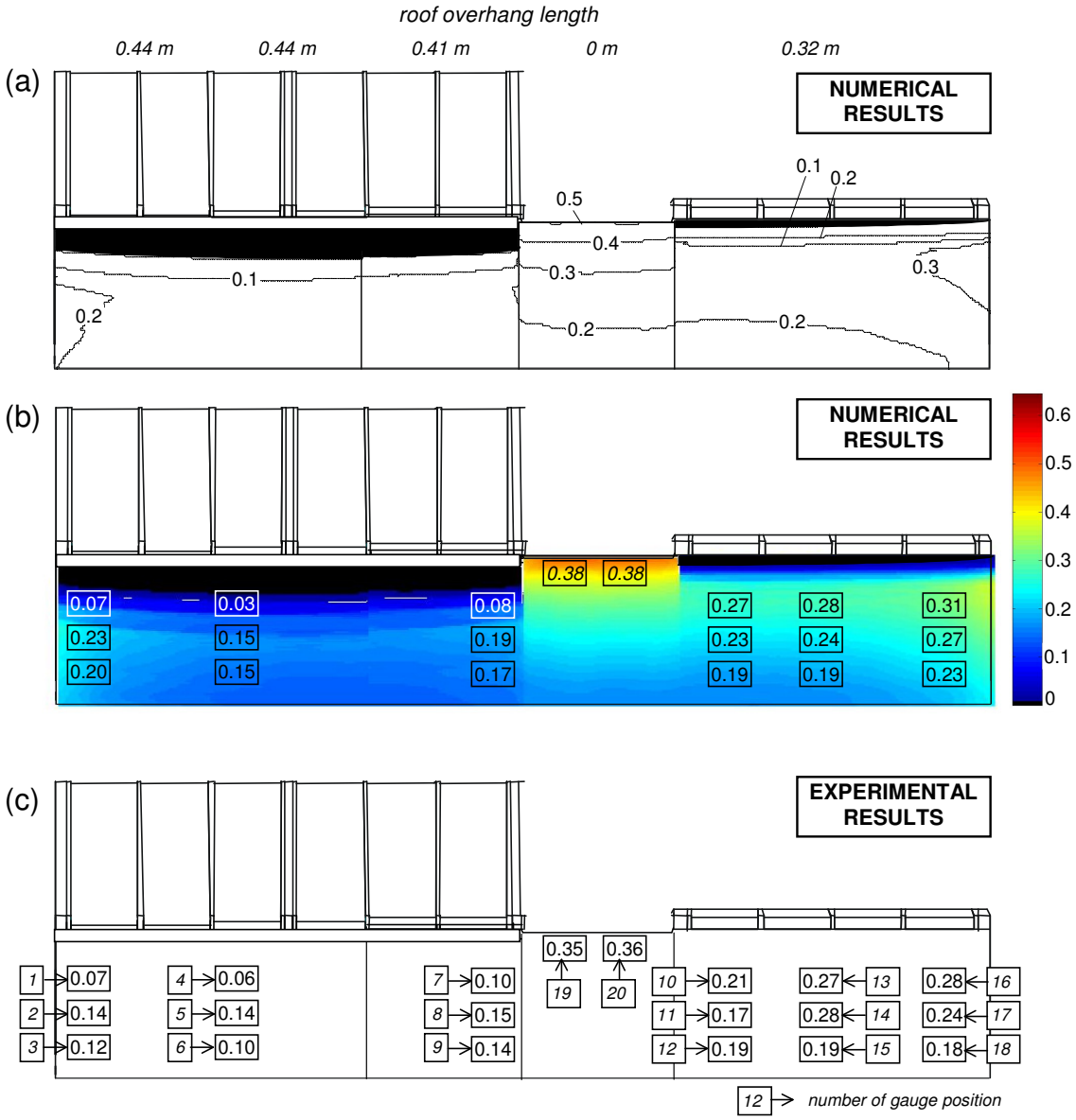

Fig. 14. Spatial distribution of the ratio S_{wdr}/S_h (total wind-driven rain amount to total horizontal rainfall amount) for the rain event (05-08/02/2002) (rain event is illustrated in Fig. 13a). The total horizontal rainfall amount S_h = 11.3 mm. (a-b) Numerical results. In Fig. 14b, the calculated ratios at the location of the wind-driven rain gauges are additionally indicated. (c) Experimental results.

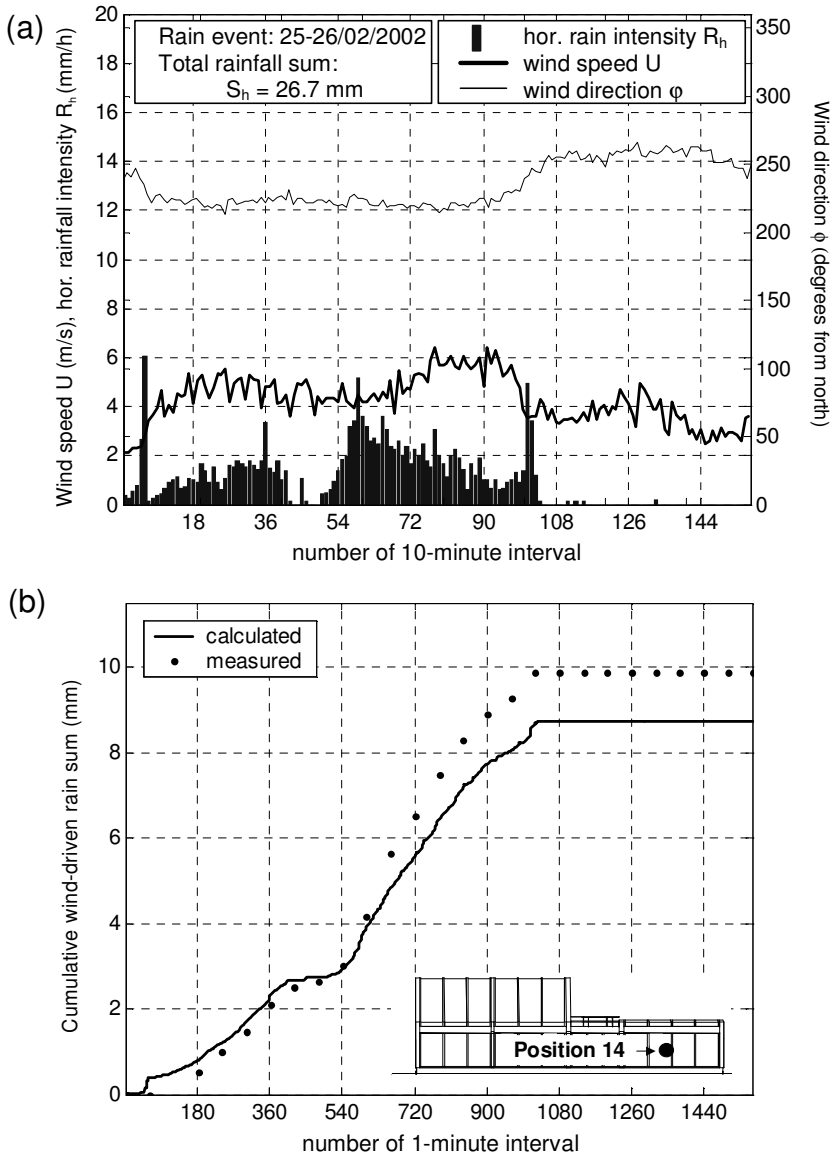

Fig. 15. (a) Meteorological data (reference wind speed, wind direction, horizontal rainfall intensity) measured during the rain event (25-26/02/2002). Total horizontal rainfall amount S_h = 26.7 mm. (b) Temporal distribution of the experimentally and numerically determined cumulative wind-driven rain amount at position 14 of the south-west facade.

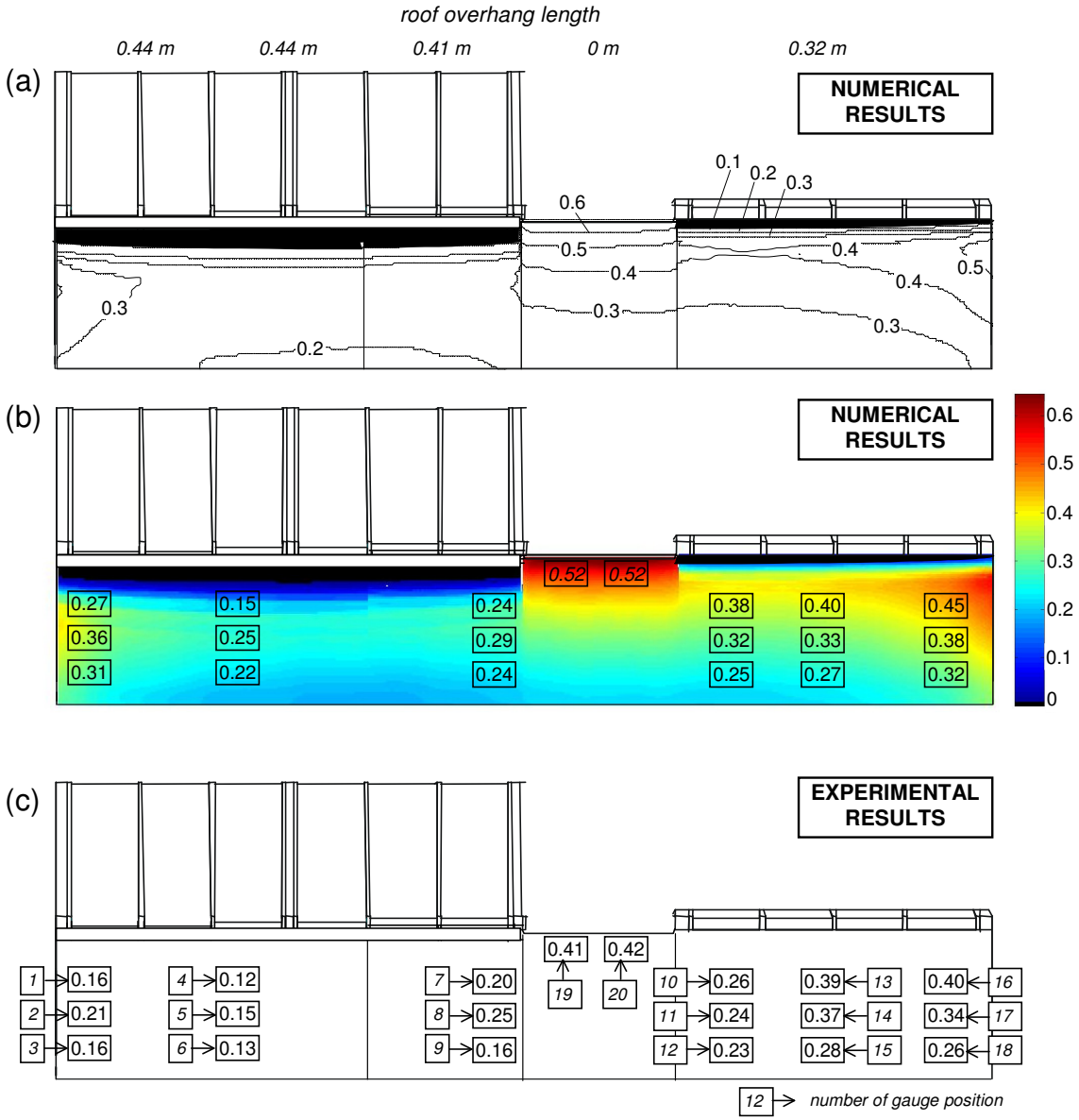

Fig. 16. Spatial distribution of the ratio S_{wdr}/S_h (total wind-driven rain amount to total horizontal rainfall amount) for the rain event (25-26/02/2002) (rain event is illustrated in Fig. 15a). The total horizontal rainfall amount S_h = 26.7 mm. (a-b) Numerical results. In Fig. 16b, the calculated ratios at the location of the wind-driven rain gauges are additionally indicated. (c) Experimental results.

Table 1: Grid characteristics for grid-convergence study

Grid name	CVs (total number)	refinement ratio
Grid1	208612	-
Grid2	459613	1.301
Grid3	1017518	1.303

Table 2: Characteristics and settings for the CFD simulation of wind flow around the VLIET test building

Fluid			
air, incompressible, viscous			
density	1.225 kg/m³		
viscosity	1.46E-05 m²/s		
static pressure	101320 Pa		
Computational domain and mesh			
Geometry			
length	212.2 m		
height	50 m		
width	89.2 m		
Building model			
dimensions:	see Fig. 1		
distance from boundaries			
upstream	80 m		
downstream	125 m		
side	32 m		
top	42.1 m		
blockage ratio	3.4 %		
Mesh			
type: unstructured			
CV type: tetrahedral			
number of CVs	1017518		
CV size on build.	0.04 to 0.3 m		
min. CV size	0.04 m		
max. CV size	6 m		
$y_P \approx$	0.01 to 0.25 m		
Model			
Turbulence model			
type	realizable k-ε [16]		
constants			
$C_{2\varepsilon}$	1.9		
σ_κ	1		
σ_ε	1.2		
Wall functions			
type	standard [17]		
constants			
κ	0.42		
E	9.81		
Boundary conditions			
Inlet			
wind speed			
type	power-law (α_P = 0.176)		
U_{10}	10 m/s		
u^*_{ABL} (fitted)	0.69 m/s		
κ	0.42		
y_0 (fitted)	0.03 m		
k	$1.5(u^*_{ABL}{}^2)$		
ε	$(u^*_{ABL}{}^3)/(\kappa(y+y_0))$		
Outlet			
type	pressure outlet		
static press.	101320 Pa		
Ground surface			
type	wall		
method	standard wall funct. [17]		
K_S	$= y_0 = 0.03$ m		
C_{Ks}	0.5		
Top			
type	symmetry		
Operating conditions			
static pressure	101320 Pa		
Solver			
segregated, steady, implicit, double pr.			
pressure interpolation: standard			
momentum: 2nd order upwind			
pressure-velocity coupling: SIMPLE			
k: 2nd order upwind			
ε: 2nd order upwind			